Monthly Notices of the ROYAL ASTRONOMICAL SOCIETY

MNRAS **522,** 6024–6034 (2023) https://doi.org/10.1093/mnras/stad1384
Advance Access publication 2023 May 8

# Constraints on $f(T)$ cosmology with Pantheon+

Rebecca Briffa [1,2]★ Celia Escamilla-Rivera,[3] Jackson Levi Said [1,2] and Jurgen Mifsud[1,2]

[1]*Institute of Space Sciences and Astronomy, University of Malta, Msida, MSD 2080, Malta*
[2]*Department of Physics, University of Malta, Msida, MSD 2080, Malta*
[3]*Instituto de Ciencias Nucleares, Universidad Nacional Autónoma de México, Circuito Exterior C.U., A.P. 70-543, México D.F. 04510, México*

Accepted 2023 May 4. Received 2023 May 4; in original form 2023 April 5

## ABSTRACT

$f(T)$ cosmology has shown promise in explaining aspects of cosmic evolution. In this work, we analyse constraints on leading models of $f(T)$ gravity in the context of the recently released Pantheon+ data set, together with comparisons with previous releases. We also consider other late time data sets including cosmic chronometers and baryonic acoustic oscillation data. Our main result is that we find that the different $f(T)$ models under investigation connect to a variety of Hubble constant, which may help alleviate the cosmic tension on this parameter.

**Key words:** cosmological parameters – dark energy.

## 1 INTRODUCTION

Cold dark matter (ΛCDM) model has been supported by unprecedented observational evidence at all cosmic scales for several decades as the standard model of cosmology (Misner, Thorne & Wheeler 1973a; Clifton et al. 2012) with ΛCDM acting as a stabilizing agent in galaxies (Bertone, Hooper & Silk 2005; Baudis 2016), and dark energy realized through the cosmological constant (Peebles & Ratra 2003; Copeland, Sami & Tsujikawa 2006). However, despite great efforts, internal consistency issues persist in the cosmological constant description of cosmology (Weinberg 1989), while direct measurements of any dark matter particles remains elusive (Gaitskell 2004). More recently, the effectiveness of the ΛCDM model has come into question with the appearance of statistical tensions between some cosmic surveys which has taken the form of the so-called $H_0$ tension (Di Valentino et al. 2021b). One perspective of the discrepancy is between model-independent measurements of the Hubble parameter at late times (Riess et al. 2019; Wong et al. 2019) and the predictive power of the ΛCDM model using early time measurements (Ade et al. 2016; Aghanim et al. 2018), or it may be an artefact of some types of measurements (Riess 2019; de Jaeger et al. 2020; Pesce et al. 2020). Ultimately, the issue may even take new types of measurements to fully resolve the possible extent of the tension such as through gravitational wave standard sirens (Amaro-Seoane, Audley et al. 2017; Baker et al. 2019; Barack et al. 2019).

The growing pressure on the ΛCDM model (Bernal, Verde & Riess 2016; Di Valentino et al. 2021a,b) has prompted a re-exploration of possible alternatives to its fundamental formulation (Sotiriou & Faraoni 2010; Clifton et al. 2012; Dainotti et al. 2021; Krishnan et al. 2021; Saridakis et al. 2021; Colgáin et al. 2022; Ren et al. 2022; Malekjani et al. 2023). These alternatives are largely built on correction terms to the Einstein–Hilbert action where the gravitational field continues to be communicated by the curvature associated with the Levi–Civita connection (Misner, Thorne & Wheeler ; Nakahara 2003). On the other hand, there is a growing body of work that considers torsion rather than curvature as the mode by which gravity is exhibited on manifolds (Aldrovandi & Pereira 2013; Cai et al. 2016; Krssak et al. 2019; Bahamonde et al. 2021). Teleparallel gravity (TG) embodies the breadth of theories in which gravity is based on the torsion associated with the teleparallel connection. The teleparallel connection is curvature-less and satisfies metricity, and so all measures of curvature identically vanish irrespective of the components of the metric. One consequence of this exchange of connections is that the Ricci scalar, as calculated using the curvature-less teleparallel connection, will vanish, i.e. $R = 0$, while its regular form $\mathring{R}$ (over-circles represent objects calculated with the Levi–Civita connection) will naturally remain arbitrary in value. Analogous to the Ricci scalar, TG produces a torsion scalar $T$ which is equal to the regular Ricci scalar up to a total divergence term $B$, making the action based on the linear form of the torsion scalar dynamically equivalent to general relativity (GR), also called the teleparallel equivalent of general relativity (TEGR).

As in curvature-based gravity models, TEGR can be modified to form different extensions to standard gravity. In fact, TEGR can be directly generalized to form $f(T)$ gravity (Ferraro & Fiorini 2007, 2008; Bengochea & Ferraro 2009; Linder 2010; Chen et al. 2011; Paliathanasis, Levi Said & Barrow 2018; Bahamonde, Flathmann & Pfeifer 2019; Bahamonde, Levi Said & Zubair 2020; Farrugia, Levi Said & Finch 2020; Bahamonde et al. 2022), which is a second order gravitational theory that has shown promise in meeting some observational challenges in both the cosmological and astrophysical sectors (Iorio & Saridakis 2012; Cai et al. 2016; Farrugia & Levi Said 2016; Farrugia, Levi Said & Ruggiero 2016; Deng 2018; Finch & Said 2018). For instance, in Nesseris et al. (2013) and Anagnostopoulos, Basilakos & Saridakis (2019) both expansion and growth data sets are used to constrain prominent models within $f(T)$ gravity. $f(T)$ gravity has also been explored using the cosmic microwave background (CMB) power spectrum in Nunes,

★ E-mail: rebecca.briffa.16@um.edu.mt

Pan & Saridakis (2018) for a power-law model. While in Benetti, Capozziello & Lambiase (2020), big bang nucleosynthesis data was used to constrain other models.

In addition to the public data sets, survey results can also be used in conjunction as priors to further analyse their consistency with said data sets. For instance, in Riess et al. (2019) the SH0ES Team estimates the Hubble constant to be $73.30 \pm 1.04\,\mathrm{km\,s^{-1}\,Mpc^{-1}}$ which was reported using Type Ia supernova events (SNIa), while the H0LiCOW Collaboration's (Wong et al. 2019) measurement of $73.3^{+1.7}_{-1.8}\,\mathrm{km\,s^{-1}Mpc^{-1}}$ relies on strong lensing from quasars. One of the lowest reported local values of the Hubble constant comes from measurements based on using the tip of the red giant branch as a standard candle with $H_0 = 69.8 \pm 1.9\,\mathrm{km\,s^{-1}Mpc^{-1}}$ as reported in Freedman et al. (2019). Together with cosmic chronometer (CC), SNIa, and baryonic acoustic oscialltions, the impact of these priors on the most studied $f(T)$ gravity models was recently studied in Briffa et al. (2022). The SNIa data set used in this study relied on the Pantheon release (PN) which is a compilation of 1048 SNIa relative luminosity distance measurements spanning the redshift range of $0.01 < z < 2.3$ (Scolnic et al. 2018a). More recently the Pantheon+ data ($\mathrm{PN^+}$ & SH0ES) set has been released which builds on the Pantheon data set and features 1701 events with a much higher concentration of data points at lower redshift bins (Riess et al. 2022; Scolnic et al. 2022; Brout et al. 2022b). This drastic increase in data points may yield much stronger constraints on cosmological models beyond ΛCDM such as $f(T)$ gravity models.

In this work, we perform constraint analyses using $\mathrm{PN^+}$ & SH0ES for the most promising $f(T)$ gravity models which we then compare with previous studies using other data sets. This lets us compare the impact of $\mathrm{PN^+}$ & SH0ES with the PN data set. We start by first reviewing some technical details of TG in Section 2, which is then followed by a description of the data sets being used in Section 3. Our main results can be found in Section 4 where we constrain our $f(T)$ gravity models using these data sets. We also present a comparison of our analyses with the standard model of cosmology in Section 5. Finally, we summarize our main results and discuss possible future work in Section 6.

## 2 TELEPARALLEL COSMOLOGY

TG is sourced by the exchange of the curvature-based Levi–Civita connection $\mathring{\Gamma}^{\sigma}{}_{\mu\nu}$ (over-circles are used throughout to denote objects determined using the Levi–Civita connection) with the teleparallel connection $\Gamma^{\sigma}{}_{\mu\nu}$ (Hayashi & Shirafuji 1979; Aldrovandi & Pereira 2013; Bahamonde et al. 2021). The curvature-less nature of the teleparallel connection means that all curvature-based geometric bodies will vanish identically (the regular curvature-based objects remain arbitrary when calculated using the Levi–Civita connection) when calculated using this connection, and so new objects are needed to build gravitational theories (Aldrovandi & Pereira 2013; Cai et al. 2016; Krssak et al. 2019).

Curvature-based gravitational models are largely built on the metric tensor, while TG is most directly expressed through the tetrad $e^{A}{}_{\mu}$ (and its inverses $E_{A}{}^{\mu}$) and spin connection $\omega^{A}{}_{B\mu}$. The tetrad $e^{A}{}_{\mu}$ builds up to the metric through

$$g_{\mu\nu} = e^{A}{}_{\mu} e^{B}{}_{\nu} \eta_{AB}\,, \quad \eta_{AB} = E_{A}{}^{\mu} E_{B}{}^{\nu} g_{\mu\nu}\,, \tag{1}$$

where Latin indices represent coordinates on the tangent space while Greek indices represent coordinates on the general manifold (Cai et al. 2016). In GR, the appearance of tetrads is not as prominent as in TG since the tetrad is not the only non-inertial variable in that description of gravity in GR. As with the metric, the tetrad observes orthogonality conditions, namely

$$e^{A}{}_{\mu} E_{B}{}^{\mu} = \delta^{A}_{B}\,, \quad e^{A}{}_{\mu} E_{A}{}^{\nu} = \delta^{\nu}_{\mu}\,, \tag{2}$$

for internal consistency. The spin connection $\omega^{A}{}_{B\mu}$ is a flat spin connection and is responsible for incorporating the local Lorentz transformation invariance into the equations of motion, which arises due to the appearance of the tangent space indices.

The tetrad and spin connection define the teleparallel connection through (Weitzenböock 1923; Krssak et al. 2019)

$$\Gamma^{\sigma}{}_{\nu\mu} := E_{A}{}^{\sigma} \left(\partial_{\mu} e^{A}{}_{\nu} + \omega^{A}{}_{B\mu} e^{B}{}_{\nu}\right)\,. \tag{3}$$

Together, the tetrad and spin connection represent the gravitational and local degrees of freedom of the system, and retain the diffeomorphism and local Lorentz invariance of the equations of motion. Analogous to the way in which the Levi-Civita connection builds up to the Riemann tensor, the torsion tensor can be constructed from the teleparallel connection as (Hayashi & Shirafuji 1979)

$$T^{\sigma}{}_{\mu\nu} := 2\Gamma^{\sigma}{}_{[\nu\mu]}\,, \tag{4}$$

where square brackets denote an antisymmetric operator. Considering a particular contraction of the torsion tensor, a torsion scalar can be put together (Aldrovandi & Pereira 2013; Cai et al. 2016; Krssak et al. 2019; Bahamonde et al. 2021)

$$T := \frac{1}{4} T^{\alpha}{}_{\mu\nu} T_{\alpha}{}^{\mu\nu} + \frac{1}{2} T^{\alpha}{}_{\mu\nu} T^{\nu\mu}{}_{\alpha} - T^{\alpha}{}_{\mu\alpha} T^{\beta\mu}{}_{\beta}\,, \tag{5}$$

which is equal to the curvature-based Ricci scalar up to a total divergence term. Thus, the TEGR action is represented by a linear Lagrangian form of the torsion scalar since (Bahamonde, Böhmer & Wright 2015; Farrugia & Levi Said 2016)

$$R = \mathring{R} + T - B = 0\,, \tag{6}$$

where $R \equiv 0$ since the teleparallel connection is curvature-less, while $\mathring{R} \neq 0$ since this is determined using the Levi-Civita connection, while the boundary term $B$ is a total divergence term. Thus, the Einstein–Hilbert action is dynamically equivalent to the representation of a linear torsion scalar which guarantees identical equations of motion for the two actions.

As curvature-based gravity, modification of TEGR can be designed and explored, with the most direct being the arbitrary generalization of the TEGR Lagrangian to $f(T)$ gravity, which we parameterize as $f(T) = -T + \mathcal{F}(T)$ gravity by raising the TEGR action (Ferraro & Fiorini 2007, 2008; Bengochea & Ferraro 2009; Linder 2010; Chen et al. 2011; Rezaei Akbarieh & Izadi 2019) through the action

$$\mathcal{S}_{\mathcal{F}(T)} = \frac{1}{2\kappa^2} \int \mathrm{d}^4x\; e\,(-T + \mathcal{F}(T)) + \int \mathrm{d}^4x\; e\mathcal{L}_{\mathrm{m}}\,, \tag{7}$$

where $\kappa^2 = 8\pi G$, $\mathcal{L}_{\mathrm{m}}$ is the matter Lagrangian, and $e = \det\left(e^{a}{}_{\mu}\right) = \sqrt{-g}$ is the tetrad determinant. A healthy TEGR exists for the case when $\mathcal{F}(T) \to 0$ and the ΛCDM model is obtained when this functional tends to a constant Λ value. The $\mathcal{F}(T)$ equations of motion are particular in that they are generically second order in nature and so do not exhibit any Gauss–Ostrogadsky ghosts (Aldrovandi & Pereira 2013). Indeed, the field equations can be written through

$$\begin{aligned} W_{a}{}^{\mu} :=\; & e^{-1}\partial_{\nu}\left(e E_{a}{}^{\rho} S_{\rho}{}^{\mu\nu}\right)(-1 + \mathcal{F}_T) - E_{a}{}^{\lambda} T^{\rho}{}_{\nu\lambda} S_{\rho}{}^{\nu\mu}\,(-1 + \mathcal{F}_T) \\ & + \frac{1}{4} E_{a}{}^{\mu}\,(-T + \mathcal{F}(T)) \\ & + E_{a}{}^{\rho} S_{\rho}{}^{\mu\nu} \partial_{\nu}(T)\,\mathcal{F}_{TT} \\ & + E_{b}{}^{\lambda} \omega^{b}{}_{a\nu} S_{\lambda}{}^{\nu\mu}\,(-1 + \mathcal{F}_T) = \kappa^2 E_{a}{}^{\rho} \Theta_{\rho}{}^{\mu}\,, \end{aligned} \tag{8}$$

where subscripts denote derivatives ($\mathcal{F}_T = \partial\mathcal{F}/\partial T$ and $\mathcal{F}_{TT} = \partial^2\mathcal{F}/\partial T^2$), and $\Theta_{\rho}{}^{\nu}$ is the regular energy–momentum tensor, and

the superpotential is defined as (Bahamonde et al. 2021)

$$S_\rho{}^{\mu\nu} = K^{\mu\nu}{}_\rho - \delta^\mu_\rho T_\sigma{}^{\sigma\nu} + \delta^\nu_\rho T_\sigma{}^{\sigma\mu} = -S_\rho{}^{\nu\mu}\,, \tag{9}$$

where the contortion tensor represents the difference between the Levi–Civi and teleparallel connections, given by

$$K^\rho{}_{\mu\nu} := \Gamma^\rho{}_{\mu\nu} - \mathring{\Gamma}^\rho{}_{\mu\nu} = \frac{1}{2}\left(T_\mu{}^\rho{}_\nu + T_\nu{}^\rho{}_\mu - T^\rho{}_{\mu\nu}\right)\,. \tag{10}$$

The individual tetrad and spin connection field equations are then represented by

$$W_{(\mu\nu)} = \kappa^2\Theta_{\mu\nu}\,, \quad \text{and} \quad W_{[\mu\nu]} = 0\,. \tag{11}$$

For any metric, a unique tetrad–spin connection pairs exist that are compatible with a vanishing spin connection, called the Weitzenböck gauge (Krssak et al. 2019; Bahamonde et al. 2021). Here, $W_{[\mu\nu]}$ vanishes identically while continuing to satisfy the metric equations in equation (1).

A flat homogeneous and isotropic cosmology is explored in this work through the tetrad (Tamanini & Boehmer 2012; Krššák & Saridakis 2016)

$$e^A{}_\mu = \mathrm{diag}\,(1,\, a(t),\, a(t),\, a(t))\,, \tag{12}$$

where $a(t)$ is the scale factor in cosmic time $t$, which was shown to universally satisfy the Weitzenböck gauge conditions in Hohmann et al. (2019). The regular flat Friedmann–Lemaître–Robertson–Walker metric is reproduced using equation (1) so that the line element takes the regular form (Misner et al. )

$$\mathrm{d}s^2 = \mathrm{d}t^2 - a^2(t)\left(\mathrm{d}x^2 + \mathrm{d}y^2 + \mathrm{d}z^2\right)\,, \tag{13}$$

from which we can define the regular Hubble parameter as $H = \dot{a}/a$, where over-dots refer to derivatives with respect to cosmic time. Using equations (4) and (6), it turns out that $T = -6H^2$ and $B = -6\left(3H^2 + \dot{H}\right)$. Thus, the $f(T)$ gravity Friedmann equations can be written as (Bahamonde et al. 2021)

$$H^2 + \frac{T}{3}\mathcal{F}_T - \frac{\mathcal{F}}{6} = \frac{\kappa^2}{3}\rho\,, \tag{14}$$

$$\dot{H}\left(1 - \mathcal{F}_T - 2T\mathcal{F}_{TT}\right) = -\frac{\kappa^2}{2}\left(\rho + p\right)\,, \tag{15}$$

where we denote the energy density and pressure of the total matter sector by $\rho$ and $p$, respectively.

## 3 OBSERVATIONAL DATA

In this study, we consider the most favourable $f(T)$ models and test them against different combinations of observational data sets. For each $f(T)$ model and data set combination, we perform an Monte Carlo Markov Chain (MCMC) analysis using the publicly available EMCEE package available at Foreman-Mackey et al. (2013). The MCMC sampler constrains the model and cosmological parameters by varying them in a range of conservative priors and exploring the posteriors of the parameter space. Therefore, for each parameter, we obtain its one- and two-dimensional distributions, where the one-dimensional distribution represents the parameters' posterior distribution whilst the two-dimensional one illustrates the covariance between two different parameters. These are complemented with their respective $1\sigma$ and $2\sigma$ confidence levels as shown in Section 4. In turn, this allows us to compare the different data sets and analyse the effects of PN$^+$ & SH0ES with the PN data set.

We devote this section to present and describe the observational data which will be considered in the analyses below based on the MCMC analysis. Our baseline data set consists of Hubble expansion data along with a SNIa.

**Cosmic chronometers (CCs)** – With regards to Hubble parameter data, we adopt thirty-one CC data points (Jimenez et al. 2003; Simon, Verde & Jimenez 2005; Stern et al. 2010; Moresco et al. 2012,2016; Zhang et al. 2014; Moresco 2015). This CC method involves spectroscopic dating techniques of passively evolving galaxies, which enables us to directly obtain observational values of the Hubble functions at various redshifts up to, $z \lesssim 2$. These measurements are independent of any cosmological model and the Cepheid distance scale, however, they are still associated with the modelling of the stellar ages, which is based on robust stellar population synthesis techniques. It involves the measurements of age difference between two passively evolving galaxies at two redshifts. Therefore, $\Delta z/\Delta t$ can be inferred from observations which in turn, makes it possible to compute $H(z) = -(1+z)^{-1}\Delta z/\Delta t$. Thus, CCs were found to be more reliable than any other method that is based on the absolute age determination of galaxies (Jimenez & Loeb 2002).

The corresponding $\chi^2_H$ estimator is given by

$$\chi^2_H = \sum_{i=1}^{31} \frac{\left(H(z_i,\Theta) - H_{\mathrm{obs}(z_i)}\right)^2}{\sigma^2_{\mathrm{H}}(z_i)}\,, \tag{16}$$

where $H(z_i,\Theta)$ are the theoretical Hubble parameter values at redshift $z_i$ with model parameters $\Theta$ whilst $H_{\mathrm{obs}}(z_i)$ are the corresponding Hubble data values at $z_i$ with observational error of $\sigma_H(z_i)$.

**Type Ia supernovae compilation**—The other baseline data set used for our MCMC analyses includes information obtained from Type Ia supernovae. These supernovae occur in binary star systems and are valuable for cosmological analyses because of their uniform intrinsic brightness, which allows us to use them as standard candles to measure distances to distant galaxies. To be more specific, the difference between the observed apparent magnitude of an object, $m$, and its absolute magnitude, $M$ (which is a measure of its intrinsic brightness) is defined as the distance modulus. At redshift $z_i$, the distance modulus is given as

$$\mu(z_i,\Theta) = m - M = 5\log_{10}[D_L(z_i,\Theta)] + 25\,, \tag{17}$$

where $D_L(z_i,\Theta)$ is the luminosity distance defined as

$$D_L(z_i,\Theta) = c(1+z_i)\int_0^{z_i}\frac{\mathrm{d}z'}{H(z',\Theta)}\,. \tag{18}$$

In addition, the apparent magnitude of each SNIa needs to be calibrated via an arbitrary fiducial absolute magnitude $M$ and thus, in the MCMC analyses, we can treat $M$ as a nuisance parameter by marginalizing over it. This is done by using theoretical models to predict the distance modulus for a given set of cosmological parameters and comparing these predictions to the observed values for the SNIa in the Pantheon catalogue. The cosmological parameters are then constrained by minimizing a $\chi^2$ likelihood specified by (Conley et al. 2011)

$$\chi^2_{\mathrm{SN}} = (\Delta\mu(z_i),\Theta))^T C^{-1}(\Delta\mu(z_i),\Theta))\,, \tag{19}$$

where $(\Delta\mu(z_i),\Theta)) = (\mu(z_i),\Theta) - \mu(z_i)_{\mathrm{obs}}$ and $C$ is the corresponding covariance matrix which accounts for the statistical and systematic uncertainties.

In this work, we use two SNIa data sets: the Pantheon (PN; Scolnic et al. 2018b) and Pantheon+ (PN$^+$ & SH0ES; Scolnic et al. 2022) compilations, which is a successor to the original Pantheon analysis. The main difference between the original Pantheon analysis and the Pantheon+ analysis in cosmology lies in the addition of new data sets to the latter. While the original Pantheon analysis used a

compilation of 1048 SNIa samples to study the expansion history of the Universe, the Pantheon+ analysis includes an even larger number of 1701 SNIa samples. The term 'PN$^+$ & SH0ES' as referred to in the Pantheon+ analysis in Brout et al. (2022a), incorporates the SH0ES Cepheid host distance anchors (R22; Riess et al. 2022) in the likelihood which helps to break the degeneracy between the parameters $M$ and $H_0$ when analysing SNIa alone. Additionally, the Pantheon+ analysis covers a wider redshift range of $0.01 < z < 2.5$, compared to the original Pantheon, which does not extend redshifts lower than $z < 0.01$. This expanded redshift range allows for an improved treatment of systematic uncertainties, resulting in better constrained parameters as will be illustrated in Section 4.

**Baryon acoustic oscillations** (BAO) – We also consider a joint BAO data set consisting of independent data points. This BAO data set includes measurements from the Sloan Digital Sky Survey (SDSS) main galaxy sample at $z_{\rm eff} = 0.15$ (Ross et al. 2015), the six-degree Field Galaxy Survey at $z_{\rm eff} = 0.106$ (Beutler et al. 2011), and the BOSS DR11 quasar Lyman-alpha measurement at $z_{\rm eff} = 2.4$ (du Mas des Bourboux et al. 2017). We also incorporate the angular diameter distances and $H(z)$ measurements of the SDSS-IV eBOSS DR14 quasar survey at $z_{\rm eff} = \{0.98, 1.23, 1.52, 1.94\}$ (Zhao et al. 2019), along with the SDSS-III BOSS DR12 consensus BAO measurements of the Hubble parameter and the corresponding comoving angular diameter distances at $z_{\rm eff} = \{0.38, 0.51, 0.61\}$ (Alam et al. 2017). For these two BAO data sets, we consider the full covariance matrix in our MCMC analyses.

For the BAO data sets under consideration, we compute the Hubble distance $D_{\rm H}(z)$, comoving angular diameter distance $D_{\rm M}(z)$, and volume-average distance $D_{\rm V}(z)$ using

$$D_{\rm H}(z) = \frac{c}{H(z)}, \tag{20}$$

$$D_{\rm M}(z) = (1+z)D_{\rm A}(z), \tag{21}$$

$$D_{\rm V}(z) = \left[(1+z)^2\, D_{\rm A}(z)^2 \frac{cz}{H(z)}\right]^{1/3}, \tag{22}$$

respectively, where $D_{\rm A}(z) = (1+z)^{-2} D_{\rm L}(z)$ is the angular diameter distance. Using the reported BAO results, we calculate the corresponding combination of parameters $\mathcal{G}(z_i) = D_{\rm V}(z_i)/r_{\rm s}(z_{\rm d})$, $r_{\rm s}(z_{\rm d})/D_{\rm V}(z_i)$,$D_{\rm H}(z_i)$,$D_{\rm M}(z_i)(r_{\rm s,\,fid}(z_{\rm d})/r_{\rm s}(z_{\rm d}))$,$H(z_i)(r_{\rm s}(z_{\rm d})/r_{\rm s,\,fid}(z_{\rm d}))$, $D_{\rm A}(z_i)(r_{\rm s,\,fid}(z_{\rm d})/r_{\rm s}(z_{\rm d}))$ for which the comoving sound horizon at the end of the baryon drag epoch at redshift $z_{\rm d} \approx 1059.94$ (Aghanim et al. 2020) is computed by

$$\begin{aligned} r_{\rm s}(z) &= \int_z^\infty \frac{c_s(\tilde{z})}{H(\tilde{z})}\,{\rm d}z \\ &= \frac{1}{\sqrt{3}} \int_0^{1/(1+z)} \frac{{\rm d}a}{a^2 H(a)\sqrt{1+\left[3\Omega_{b,0}/(4\Omega_{\gamma,0})\right]a}}, \end{aligned} \tag{23}$$

where we have adopted $\Omega_{b,0} = 0.02242$, $\Omega_{\gamma,0} = 2.4697 \times 10^{-5}$ (Aghanim et al. 2020), $T_0 = 2.7255$ K (Fixsen 2009), and a fiducial value of $r_{s,{\rm fid}}(z_d) = 147.78$ Mpc.

The corresponding $\chi^2$ for the BAO data is calculated using

$$\chi^2_{\rm BAO}(\Theta) = \Delta G(z_i, \Theta)^T C^{-1}_{\rm BAO} \Delta G(z_i, \Theta) \tag{24}$$

where $\Delta G(z_i, \Theta) = G(z_i, \Theta) - G_{\rm obs}(z_i)$ and $C_{\rm BAO}$ is the covariance matrix of all the considered BAO observations.

## 4 RESULTS

In this section, we present and analyse the results following the methodology outlined in Section 3 and using the observational data previously discussed. Each subsection focuses on the most promising models of $f(T)$, presenting contour plots of the constrained parameters with $1\sigma$ and $2\sigma$ uncertainties, along with corresponding tables with final results. These models have gained prominence in literature and are frequently studied due to their ability to mirror very well our cosmological history. In all tables and posterior plots, we include results of the Hubble constant $H_0$, the current matter density parameter $\Omega_{m,0}$ together with the model parameters. This will allow us to analyse how the different independent data sets and cosmological models impact the Hubble tension. We also provide a brief discussion of the most noteworthy findings, highlighting the differences between the PN and PN$^+$ & SH0ES.

### 4.1 Power Law Model

The power-law model, henceforth referred to as $f_1$CDM, which was introduced by Bengochea & Ferraro (2009), proposes an alternative explanation for the observed acceleration of the late-time Universe that does not involve dark energy. The model introduces a modification function $\mathcal{F}_1(T)$, which has a power-law form with two constant parameters $\alpha_1$ and $p_1$ specified by

$$\mathcal{F}_1(T) = \alpha_1(-T)^{p_1}, \tag{25}$$

The constant $\alpha_1$ can be calculated using the Friedman equation equation (14) at current times

$$\alpha_1 = \left(6H_0^2\right)^{1-p_1} \frac{1-\Omega_{m,0}-\Omega_{r,0}}{1-2p_1}, \tag{26}$$

where $\Omega_{m,0}$ and $\Omega_{r,0}$ are the density parameter for matter and radiation at current times, respectively. Thus, instead of introducing two new parameters as in the original equation, only one new model parameter, $p_1$, is required for the $f_1$CDM model, making it a simpler and more elegant model. The value of $p_1$ can be obtained by applying the MCMC analyses to observational data.

The Friedmann equation for the $f_1$CDM model can, therefore, be obtained by substituting the above equation in equation (14) such that

$$E^2(z) = \Omega_{m,0}(1+z)^3 + \Omega_{r,0}(1+z)^4 + (1-\Omega_{m,0}-\Omega_{r,0})E^{2p_1}(z), \tag{27}$$

which is not solvable analytically in terms of the normalized Hubble parameter $E(z) := \frac{H(z)}{H_0}$. For this reason, we must utilize numerical methods to determine the value of $E(z)$ at each redshift point. Thus, for each iteration of the MCMC analysis, we solve for each redshift point at which observations exist. It is worth noting that for $p_1 = 0$, equation (27) reduces to $\Lambda$CDM, whereas for $p_1 = 1$, the GR limit is recovered as the additional component in the Friedmann equation produces a rescaled gravitational constant term in the density parameters. The objective is to obtain values of $H_0$, $\Omega_{m,0}$, and $p_1$ that provide the best fit to the observational data using the MCMC analyses.

The constraints on the specified parameters for $f_1$CDM model are shown in Fig. 1. The figure shows both the confidence regions and the posteriors for different combinations of observational data sets. Specifically, the figure shows the results for data sets that include either the PN catalogue or the PN$^+$ & SH0ES. Upon closer examination of the posteriors, it is evident that the parameters from the data set combinations that include PN$^+$ & SH0ES exhibit tighter constraints, with the $H_0$ parameter showing notably improved precision. On the other hand, the contour plots for the CC+PN and CC+PN$^+$ & SH0ES data set combinations display a degeneracy between the $H_0$ parameter and the $p_1$ parameter. However, once the BAO data set is included

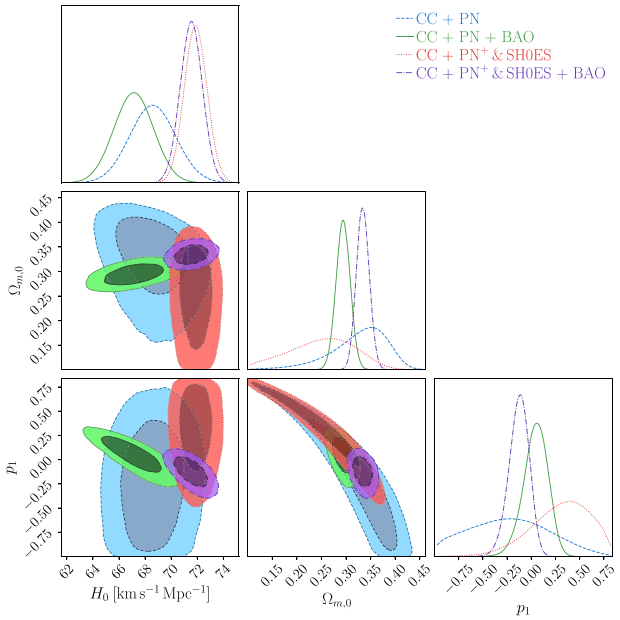


**Figure 1.** Confidence contours and posteriors for $f_1$CDM for the parameters $H_0$, $\Omega_{m,0}$, and $p_1$. The blue and green contours represent data set combinations that include PN data set, while the red and purple contours show combinations that also include the PN$^+$ & SH0ES data sets.

this degeneracy breaks and reveals an anti-correlation between the two parameters. It is noteworthy that the CC+PN$^+$ & SH0ES data set combination shows a degeneracy between the $\Omega_{m,0}$ parameter and $H_0$, while for all data set combinations an anti-correlation is observed between the $p_1$ parameter and the $\Omega_{m,0}$ parameter. However, the strength of this anti-correlation is less pronounced for the data sets that include the BAO.

The precise values for the cosmological and model parameters, including the nuisance parameter $M$, for $f_1$CDM are shown in Table 1. It becomes clear that the values of $H_0$ for the data set combinations that include PN$^+$ & SH0ES are relatively higher than their corresponding $H_0$ values. This finding is consistent with the high value of $H_0$ obtained by the SH0ES team (R22), which reports $H_0 = 73.30 \pm 1.04\,\mathrm{km\,s^{-1}\,Mpc^{-1}}$ (Riess et al. 2022). The results show that the highest values of $H_0$ are obtained for the CC+PN$^+$ & SH0ES with a value of $H_0 = 71.88^{+0.87}_{-0.89}\,\mathrm{km\,s^{-1}Mpc^{-1}}$. Interestingly, in this scenario the $\Omega_{m,0}$ parameter reaches a minimum value, implying that most of the energy in the Universe appears as an effective dark energy, in line with the high value of $H_0$.

The inclusion of PN appears to better constrain the values of $p_1$, and this effect is even more pronounced with the addition of the BAO data. However, for the PN$^+$ & SH0ES data set, the $p_1$ parameter is found to be within $1\sigma$ of the corresponding $\Lambda$CDM value, whereas it moves to $2\sigma$ for the PN$^+$ & SH0ES combination.

The next section will provide a more detailed statistical analysis of these findings, including a comparison with the $\Lambda$CDM model.

### 4.2 Linder Model

The Linder model, henceforth referred to as $f_2$CDM, was specifically designed to account for the late-time acceleration of the Universe without the need for dark energy. This model incorporates a torsion scalar, $T$, and is described by the equation

$$\mathcal{F}_2 = \alpha_2 T_0 \left(1 - \exp\left[-p_2\sqrt{T/T_0}\right]\right), \tag{28}$$

where $\alpha_2$ and $p_2$ are constants and $T_0$ represents the current value of the torsion scalar, that is $T|_{t=t_0} = -6H_0^2$. The constant $\alpha_2$ can be determined by evaluating the Friedmann equation at current times, which gives

$$\alpha_2 = \frac{1 - \Omega_{m,0} - \Omega_{r,0}}{(1 + p_2)e^{-p_2} - 1}. \tag{29}$$

Therefore, the only new model parameter in the $f_2$CDM model is $p_2$. Using the above equations, the Friedmann equation for this model can be defined as

$$E^2(z) = \Omega_{m,0}(1+z)^3 + \Omega_{r_0}(1+z)^4 + \frac{1 - \Omega_{m,0} - \Omega_{r_0}}{(p_2+1)e^{-pb_2} - 1} \left[(1 + p_2 E(z))\exp\left[-p_2 E(z)\right] - 1\right]. \tag{30}$$

This model can be reduced to $\Lambda$CDM when $p_2 \to \infty$. However, to ensure numerical stability, the analysis is performed for $1/p_2$, so that this limit becomes $1/p_2 \to 0^+$.

In Fig. 2, the posterior and confidence levels of the constrained parameters for $f_2$CDM are displayed. The blue and green contours correspond to the combination of data sets that includes the PN sample, whereas the red and purple contours represent the combinations that consist of the PN$^+$ & SH0ES samples. The $f_2$CDM model shows similar trends to the $f_1$CDM model, with tighter constraints for PN$^+$ & SH0ES, particularly for the Hubble constant $H_0$, especially when the BAO data set is included. The CC+PN$^+$ & SH0ES+BAO data set is the most constrained, indicating the highest precision. The anti-correlation between $\Omega_{m,0}$ and $\frac{1}{p_2}$ parameters remains evident in this model, particularly for data sets including the PN$^+$ & SH0ES catalogue.

Table 2 presents the exact numerical values of the parameters shown in Fig. 2, including the nuisance parameter $M$. The results show that the estimated values of $H_0$ are comparable to those obtained in the $f_1$CDM model. However, as the $f_2$CDM model is specifically designed to predict an accelerating Universe in the late-time regime, the inferred values of the matter density parameter $\Omega_{m,0}$ are slightly lower compared to the previous model. Therefore, in this case, the $p_2$ parameter in the exponential term is allowing for a more flexible description of the Universe, and the data constraints favour a lower matter density to be consistent with the observed acceleration. The

**Table 1.** Results for the $f_1$CDM (power law) model, where the first column lists the data sets used to constrain the parameters. The second to fourth columns display the constrained parameters, namely $H_0$, $\Omega_{m,0}$, and $p_1$, while the last column shows the nuisance parameter $M$.

| Data sets | $H_0$ [km s$^{-1}$ Mpc$^{-1}$] | $\Omega_{m,0}$ | $p_1$ | $M$ |
|---|---|---|---|---|
| CC+PN | $68.6^{+1.7}_{-1.8}$ | $0.352^{+0.042}_{-0.063}$ | $-0.22^{+0.41}_{-0.48}$ | $-19.390^{+0.052}_{-0.053}$ |
| CC+PN+BAO | $67.1 \pm 1.5$ | $0.294^{+0.015}_{-0.014}$ | $0.06^{+0.12}_{-0.13}$ | $-19.435 \pm 0.044$ |
| CC+PN$^+$ & SH0ES | $71.88^{+0.87}_{-0.89}$ | $0.266^{+0.062}_{-0.076}$ | $0.40^{+0.28}_{-0.33}$ | $-19.295 \pm 0.025$ |
| CC+PN$^+$ & SH0ES+BAO | $71.55^{+0.85}_{-0.86}$ | $0.334^{+0.014}_{-0.013}$ | $-0.113^{+0.098}_{-0.108}$ | $-19.309^{+0.024}_{-0.025}$ |

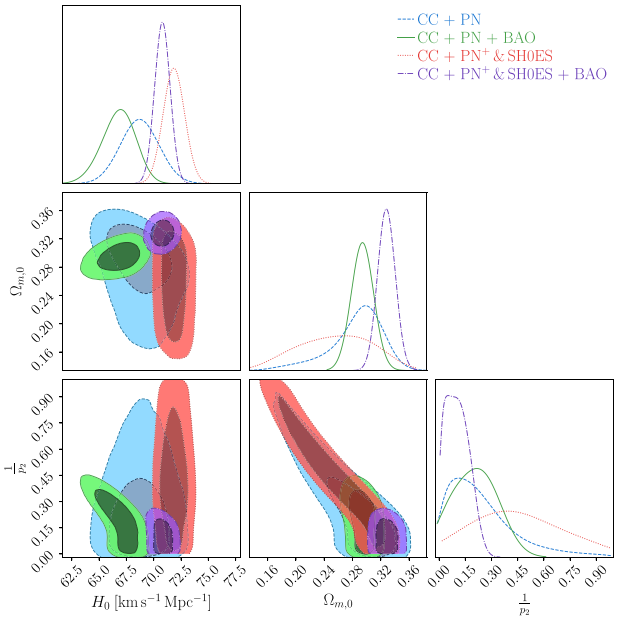


**Figure 2.** Confidence contours and posteriors for $f_2$CDM for the parameters $H_0$, $\Omega_{m,0}$, and $\frac{1}{p_2}$. The blue and green contours represent data set combinations that include PN data set, while the red and purple contours show combinations that also include the PN$^+$ & SH0ES data sets.

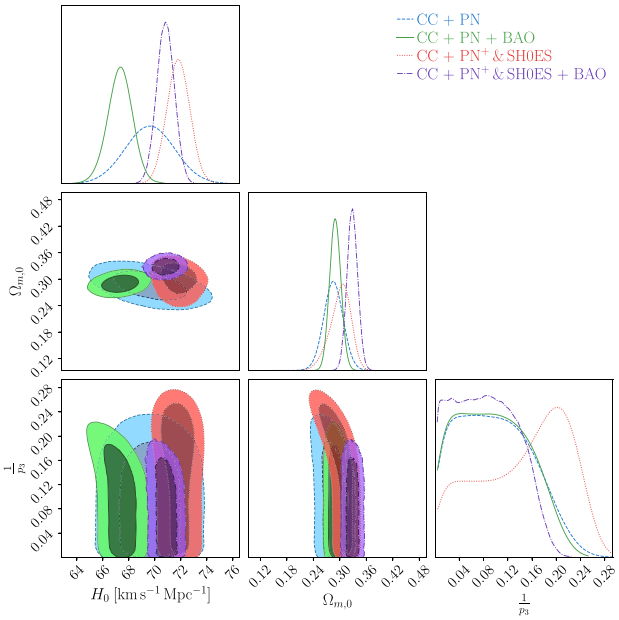


**Figure 3.** Confidence contours and posteriors for $f_3$CDM for the parameters $H_0$, $\Omega_{m,0}$, and $\frac{1}{p_3}$. The blue and green contours represent data set combinations that include PN data set, while the red and purple contours show combinations that also include the PN$^+$ & SH0ES data sets.

CC+PN$^+$ & SH0ES data set combination yields the lowest value of $\Omega_{m,0}$, which is $\Omega_{m,0} = 0.269^{+0.046}_{-0.065}$. In tandem, the highest value for the Hubble constant is obtained for the same data set combination giving a value of $H_0 = 71.86^{+0.97}_{-0.99}$ km s$^{-1}$Mpc$^{-1}$.

By design of the model itself, the parameter $\frac{1}{p_2}$ is positive throughout. In comparison to the $f_1$CDM model, the parameter values of $f_2$CDM tend to fall within $2\sigma$ of the ΛCDM limit instead of $1\sigma$. Therefore, the $f_2$CDM model is slightly further away from strongly supporting the ΛCDM model.

The inclusion of the PN$^+$ & SH0ES data set has a noticeable impact on the MCMC runs and the resulting model parameters. While the results are still in agreement with those obtained from the PN data set alone, the uncertainties in the parameters, especially the Hubble constant, are significantly reduced. This makes the PN$^+$ & SH0ES data set useful for comparative purposes with ΛCDM. Further comparisons and statistical analyses with ΛCDM are discussed in Section 5.

### 4.3 Exponential Model

The third model is motivated by works in $f(\mathring{R})$ gravity (Linder 2009), in which an exponential model is again taken into consideration. Indeed, Nesseris et al. (2013), propose a variant of the Linder model where the function $\mathcal{F}_3$ is given by an exponential function with two constants $\alpha_3$ and $p_3$ as parameters

$$\mathcal{F}_3 = \alpha_3 T_0 \left(1 - \exp\left[-p_3 T/T_0\right]\right) . \tag{31}$$

The constant $\alpha_3$ can be determined by evaluating the Friedmann equation at current times and is given by

$$\alpha_3 = \frac{1 - \Omega_{m,0} - \Omega_{r,0}}{(1 + 2p_3)e^{-p_3} - 1} . \tag{32}$$

The Friedmann equation for this model is therefore obtained using equation (14) and substituting the above equations such that

$$E^2(z) = \Omega_{m_0}(1+z)^3 + \Omega_{r_0}(1+z)^4 + \frac{1 - \Omega_{m,0} - \Omega_{r_0}}{(1 + 2p_3)e^{-p_3} - 1} \left[\left(1 + 2p_3 E^2(z)\right) \exp\left[-p_3 E^2(z)\right] - 1\right] , \tag{33}$$

The behaviour of this model is similar to $f_2$CDM in the sense that as $p_3 \to \infty$, it tends towards ΛCDM. For numerical stability, the analysis is performed in terms of $1/p_3$ instead, such that the limit of ΛCDM corresponds to $1/p_3 \to 0^+$.

The posterior and confidence levels for the $f_3$CDM model are presented in Fig. 3. Even though this model is a variant of the Linder model, the removal of the square root has had a significant impact on the constraints, in particular on the $\Omega_{m,0}$ parameter. Unlike the previous models, the degeneracy between $H_0$ and $\Omega_{m,0}$ parameters

**Table 2.** Results for the $f_2$CDM (Linder) model, where the first column lists the data sets used to constrain the parameters. The second to fourth columns display the constrained parameters, namely $H_0$, $\Omega_{m,0}$, and $\frac{1}{p_2}$, while the last column shows the nuisance parameter $M$.

| Data sets | $H_0$ [km s$^{-1}$ Mpc$^{-1}$] | $\Omega_{m,0}$ | $\frac{1}{p_2}$ | $M$ |
|---|---|---|---|---|
| CC+PN | $68.7^{+1.8}_{-1.7}$ | $0.298^{+0.031}_{-0.036}$ | $0.11^{+0.22}_{-0.11}$ | $-19.433^{+0.117}_{-0.083}$ |
| CC+PN+BAO | $66.9^{+1.5}_{-1.6}$ | $0.294 \pm 0.016$ | $0.22^{+0.12}_{-0.15}$ | $-19.38^{+0.22}_{-0.35}$ |
| CC+PN$^+$ & SH0ES | $71.86^{+0.97}_{-0.99}$ | $0.269^{+0.046}_{-0.065}$ | $0.39^{+0.29}_{-0.25}$ | $-19.287^{+0.048}_{-0.032}$ |
| CC+PN$^+$ & SH0ES+BAO | $70.79 \pm 0.71$ | $0.328^{+0.013}_{-0.012}$ | $0.052^{+0.104}_{-0.038}$ | $-19.322^{+0.026}_{-0.033}$ |

**Table 3.** Results for the $f_3$CDM model, where the first column lists the data sets used to constrain the parameters. The second to fourth columns display the constrained parameters, namely $H_0$, $\Omega_{m,0}$, and $\frac{1}{p_3}$, while the last column shows the nuisance parameter $M$.

| Data sets | $H_0$ [km s$^{-1}$ Mpc$^{-1}$] | $\Omega_{m,0}$ | $\frac{1}{p_3}$ | $M$ |
|---|---|---|---|---|
| CC+PN | $69.6^{+1.9}_{-2.0}$ | $0.286 \pm 0.022$ | $0.065^{+0.082}_{-0.050}$ | $-19.367^{+0.054}_{-0.057}$ |
| CC+PN+BAO | $67.35^{+0.94}_{-0.97}$ | $0.289 \pm 0.013$ | $0.043^{+0.101}_{-0.026}$ | $-19.441^{+0.032}_{-0.031}$ |
| CC+PN$^+$ & SH0ES | $71.80 \pm 0.89$ | $0.307^{+0.020}_{-0.026}$ | $0.201^{+0.045}_{-0.114}$ | $-19.302^{+0.033}_{-0.021}$ |
| CC+PN$^+$ & SH0ES+BAO | $70.80^{+0.70}_{-0.66}$ | $0.329 \pm 0.012$ | $0.086^{+0.035}_{-0.081}$ | $-19.259 \pm 0.077$ |

is no longer significant, but the correlation between $\Omega_{m,0}$ and $\frac{1}{p_3}$ is emphasized (for clarity we have added the prior ranges for all models in Appendix C).

The constrained values for the parameters of the $f_3$CDM model are presented in Table 3 which exhibit stricter and tighter confidence levels in the density parameter. Notably, the highest value of $H_0$ is once again obtained for the CC+PN$^+$ & SH0ES data set combination, with $H_0 = 71.80 \pm 0.89$, km s$^{-1}$Mpc$^{-1}$. The value of $H_0$ obtained for CC+PN$^+$ & SH0ES in the $f_3$CDM model is consistent with the previous corresponding values. However, the difference between the $H_0$ values for CC+PN$^+$ & SH0ES and CC+PN$^+$ & SH0ES+BAO is slightly larger than that obtained for $f_1$CDM. This implies that the value of $H_0$ for CC+PN$^+$ & SH0ES+BAO is slightly lower in the $f_3$CDM model.

With regards to the $p_3$ parameter, the resulting values are closer to the $\Lambda$CDM limit when compared to the previous model. However, the uncertainties still suggest a deviation at the $2\sigma$ level from $\Lambda$CDM. These results obtained will be further analysed and statistically compared with $\Lambda$CDM in the next section.

## 5 MODEL COMPARISON

We evaluate the performance of each $f_i$CDM model and data set by computing their respective minimum $\chi^2_{\rm min}$ values, obtained from the maximum likelihood $L_{\rm max}$ since $\chi^2_{\rm min} = -2 \ln L_{\rm max}$. Additionally, we compare the models against the standard $\Lambda$CDM by using the Akaike Information Criteria (AIC), which accounts for both the goodness of fit (measured by $\chi^2_{\rm min}$) and the complexity of the model (determined by the number of parameters $n$). The AIC is defined as

$$\mathrm{AIC} = \chi^2_{\rm min} + 2n\,. \tag{34}$$

In practice, a lower value of the AIC indicates that a model fits the data better, while also taking into account the complexity of the model. The AIC penalizes models that have more parameters, even if they provide a better fit to the data. This means that a model with a lower AIC is preferred over a model with a higher AIC, as long as the difference in AIC is significant enough.

In addition, we also examine the Bayesian Information Criterion (BIC), which is similar to AIC but it puts more weight on the complexity of the model than AIC does and is defined as

$$\mathrm{BIC} = \chi^2_{\rm min} + n \ln m\,, \tag{35}$$

where $m$ is the sample size of the observational data combination. The BIC has the same goal as the AIC, that is, to balance the fit of the model to the data against the complexity of the model. However, the BIC tends to penalize models with more parameters more heavily than AIC does as it takes the logarithm of the sample size, so the penalty for more parameters becomes more severe as the sample size increases. In practical terms, comparing the BIC values of two models can help determine which one is more supported by the data,

**Table 4.** Results for each model that include $\chi^2_{\rm min}$, AIC, BIC, and their differences relative to the $\Lambda$CDM model (i.e. $\Delta$AIC and $\Delta$BIC). The left-hand side of the table presents the results obtained from the CC+PN data sets, while the right-hand side shows the results obtained from the CC+PN$^+$ & SH0ES data sets.

| Model | CC+PN | | | CC+PN$^+$ & SH0ES | | |
|---|---|---|---|---|---|---|
| | $\chi^2_{\rm min}$ | $\Delta$AIC | $\Delta$BIC | $\chi^2_{\rm min}$ | $\Delta$AIC | $\Delta$BIC |
| $\Lambda$CDM | 1041.49 | 0 | 0 | 1548.30 | 0 | 0 |
| $f_1$CDM | 1040.94 | 1.44 | 6.43 | 1546.64 | 0.34 | 5.80 |
| $f_2$CDM | 1041.49 | 2.00 | 6.98 | 1546.67 | 0.37 | 5.82 |
| $f_3$CDM | 1045.04 | 5.54 | 10.53 | 1546.77 | 0.47 | 5.93 |

**Table 5.** Results for each model that include $\chi^2_{\rm min}$, AIC, BIC, and their differences relative to the $\Lambda$CDM model (i.e. $\Delta$AIC and $\Delta$BIC). The left-hand side of the table presents the results obtained from the CC+PN+BAO data sets, while the right-hand side shows the results obtained from the CC+PN$^+$ & SH0ES+BAO data sets.

| Model | CC+PN+BAO | | | CC+PN$^+$ & SH0ES+BAO | | |
|---|---|---|---|---|---|---|
| | $\chi^2_{\rm min}$ | $\Delta$AIC | $\Delta$BIC | $\chi^2_{\rm min}$ | $\Delta$AIC | $\Delta$BIC |
| $\Lambda$CDM | 1057.46 | 0 | 0 | 1560.68 | 0 | 0 |
| $f_1$CDM | 1057.13 | 1.68 | 6.68 | 1559.24 | 0.55 | 6.02 |
| $f_2$CDM | 1056.52 | 1.06 | 6.06 | 1560.68 | 1.99 | 7.46 |
| $f_3$CDM | 1060.55 | 5.09 | 10.09 | 1560.68 | 1.99 | 7.47 |

in which models with lower BIC values are favoured as long as the difference is sufficiently large.

To compare the performance of various models using different combinations of data sets, we calculate the differences in AIC and BIC between each model and the $\Lambda$CDM model as a reference model with which to compare. The constrained parameters for $\Lambda$CDM model for each data set combination can be found in Table A1 in the Appendix A. We compare with the $\Lambda$CDM model as a comparison between each model and the standard model of cosmology. Smaller values of $\Delta$AIC and $\Delta$BIC suggest that the model with the chosen data set is more similar to the $\Lambda$CDM model, indicating better performance. In all cases, the differences are shown with respect to the $\Lambda$CDM reference model so that $\Delta\mathrm{AIC} = \mathrm{AIC}_{f_i\mathrm{CDM}} - \mathrm{AIC}_{\Lambda\mathrm{CDM}}$, and similarly for $\Delta$BIC. Indeed, Tables 4 and 5 provide the values for various statistical measures, such as $\chi^2_{\rm min}$, $\Delta\mathrm{AIC} = \Delta\chi^2_{\rm min} + 2\Delta n$, and $\Delta\mathrm{BIC} = \Delta\chi^2_{\rm min} + \Delta n \ln m$, for each model. Specifically, Table 4 compares the models that use CC+PN with the ones that use CC+PN$^+$ & SH0ES, whereas Table 5 compares the models that use CC+PN+BAO with the ones that use CC+PN$^+$ & SH0ES+BAO.

Upon initial examination, it appears that the PN$^+$ & SH0ES results in significantly lower values of $\Delta$AIC and $\Delta$BIC, despite the higher $\chi^2_{\rm min}$ value due to the increased number of data points. It is worth noting that the $\chi^2_{\rm min}$ values for the $f(T)$ models considered are slightly lower than that of the $\Lambda$CDM model for the

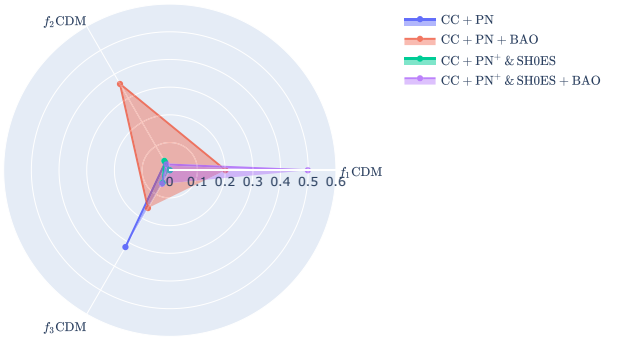


**Figure 4.** Distances, in units of standard deviations ($\sigma$), between the constrained values of $H_0$ and the $\Lambda$CDM value for different combinations of data sets, represented by different colours.

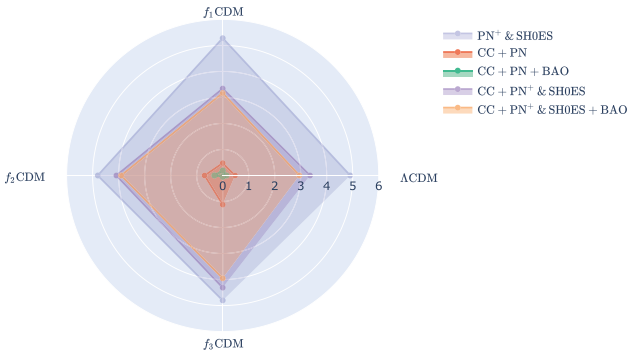


**Figure 5.** Distances, in units of standard deviations ($\sigma$), between the constrained values of $H_0$ for different combinations of data sets, represented by different colours and the P18 value.

CC+PN$^+$ & SH0ES data set. Moreover, the values of $\Delta$AIC and $\Delta$BIC for the CC+PN$^+$ & SH0ES are very close, indicating a stronger data set in which the constrained parameters are similar to those produced by the $\Lambda$CDM model. It seems that while CC+PN observations support the $\Lambda$CDM model, the inclusion of PN$^+$ & SH0ES data does not provide strong evidence in favour of the $\Lambda$CDM model over the considered $f(T)$ cosmological models given that both $\Delta$AIC and $\Delta$BIC are statistically comparable. Incorporating the BAO data set with the data sets reveals a similar trend, but to a lesser extent. However, for the $f_2$CDM model, the values for both $\Delta$AIC and $\Delta$BIC are higher for CC+PN$^+$ & SH0ES+BAO, indicating that this model is not strongly supported by the observational data in comparison to the $\Lambda$CDM model.

The previous analysis is further supported by Fig. 4, which compares the constrained $H_0$ values obtained from the $f(T)$ models to those obtained from the corresponding $\Lambda$CDM model. The figure shows that, for each data set combination represented by different colours, the $H_0$ values obtained from the $f(T)$ models are within $1\sigma$ of the corresponding $\Lambda$CDM values. The plot provides a visualization of the variations in $H_0$ estimates across different data sets, with greater distances indicating larger discrepancies between the constrained and $\Lambda$CDM values of $H_0$. Therefore, the plot suggests that the $H_0$ values obtained using the $f(T)$ models are comparable to those obtained using the $\Lambda$CDM model.

In contrast, Fig. 5 shows the difference in $\sigma$ units between the constrained $H_0$ values obtained from the MCMC analysis and the Planck 18 (P18) value of $H_0 = 67.4 \pm 0.5 \mathrm{km\,s^{-1}Mpc^{-1}}$ (Aghanim et al. 2020). In this case, we also consider the PN$^+$ & SH0ES data set on its own, for which the constrained $H_0$ values for each model are shown in Table B1 in the Appendix B. The plot clearly shows the $5\sigma$ tension between the PN$^+$ & SH0ES data set and the P18 value under the $\Lambda$CDM model. However, the inclusion of the CC data set at late-times appears to reduce the tension to around $3\sigma$–$4\sigma$ for all models. Furthermore, inclusion of the BAO data set significantly reduces this tension, as expected, since the BAO data set captures the effects of the early Universe in agreement with the Planck CMB data set.

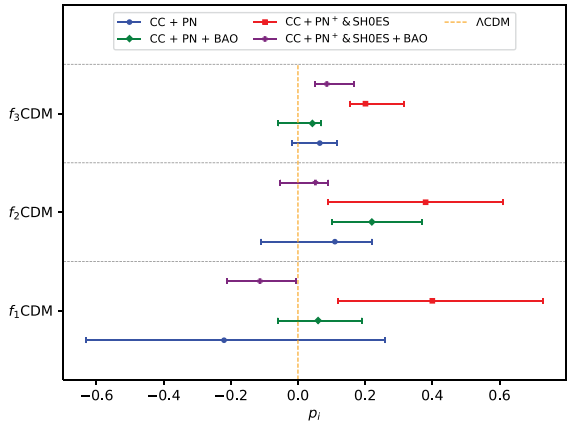


**Figure 6.** Values of the constrained model parameter $p_i$ which corresponds to $p_1$ for $f_1$CDM, $\frac{1}{p_2}$ for $f_2$CDM and $\frac{1}{p_3}$ for $f_3$CDM. Each colour represents a different data set combination while the orange line represents the $\Lambda$CDM value, i.e. $p_i = 0$.

Finally, we observe the effects that the PN$^+$ & SH0ES has on the model parameter $p_i$, in the whisker plot Fig. 6. The results indicate that the use of PN$^+$ & SH0ES leads to a more tightly constrained estimate of $p_i$ compared to other methods, as previously observed. Notably, the CC+PN and CC+PN+BAO methods produce $p_i$ values that fall within $1\sigma$ of the $\Lambda$CDM value. However, for CC+PN$^+$ & SH0ES, this is not necessarily the case as the estimated $p_i$ values do not consistently fall within $1\sigma$ of the $\Lambda$CDM value.

## 6 CONCLUSION

In this work, we have presented a constraints analysis that examines the behaviour on the parameters of the PN$^+$ & SH0ES over the PN data set. We evaluate three prominent models in $f(T)$ gravity and probe their performance against the two observational data sets by considering different data set combinations. Our primary objective was to compare the results obtained from the PN$^+$ & SH0ES data sets to those of the PN catalogue. We aimed to evaluate the differences in the outcomes of these data sets and assess their impact on the performance of the $f(T)$ gravity models under consideration. Indeed, for each model, we performed a full MCMC analysis obtaining observational constraints on the cosmological parameters for all different combinations of data. Additionally, we compared the performance of each model and data set to the standard model of cosmology using statistical indicators such as AIC and BIC. Finally, in light of the increasing tensions between cosmological observations, we have presented how the $H_0$ value compares the corresponding $\Lambda$CDM value and also with the P18 value.

We evaluated the performance of three models, namely $f_{1\text{–}3}$CDM, in which a continuous $\Lambda$CDM is present, and a specific setting

of an additional model parameter recovers a constant cosmological constant contribution. For all models, the posterior and confidence contours immediately reveal the PN$^+$ & SH0ES data set produced tighter constraints for the model parameters compared to the PN data set. Additionally, for all models considered, the PN$^+$ & SH0ES data set produced higher values of $H_0$ due to its composition of the PN$^+$ & SH0ES catalogue and the SH0ES Cepheid host distance anchors, which were consistent with previous SH0ES team results (R22). Notably, we obtained a consistent value of $H_0$ across all models for all different data set combinations. However, concerning the $\Omega_{m,0}$ parameter, $f_2$CDM and $f_3$CDM models produce lower values than the $f_1$CDM model. The additional model parameter $p_i$, for the PN data set mostly fall within $1\sigma$ of the $\Lambda$CDM model. However, with regards to PN$^+$ & SH0ES they are mostly out of the $1\sigma$ but within the $2\sigma$ range.

In Appendix A, we present the results obtained from the $\Lambda$CDM model, which we use for statistical comparisons. Our analysis revealed that the models under consideration are generally consistent with the $\Lambda$CDM model. Indeed, the statistical indicators, clearly indicate that the PN$^+$ & SH0ES is a stronger data set as the constrained parameters are close to those produced by the $\Lambda$CDM model. In addition, the information criteria $\Delta$AIC and $\Delta$BIC suggest that the CC+PN data support the $\Lambda$CDM model, whereas the PN$^+$ & SH0ES data set does not provide strong evidence that supports the $\Lambda$CDM model over the $f(T)$ cosmological models, as indicated by their relatively small values.

Finally, incorporating the CC data with the PN$^+$ & SH0ES data set reduces the $H_0$ tension to around $3\sigma$ (as illustrated in Fig. 5). Additionally, including the BAO data set also has an impact on the $H_0$ values, which are slightly reduced due to the effects from the early Universe. However, the contour plots in the triangular plots reveal an interesting point. When the BAO data set is included, the degeneracy between the parameters $H_0$ and $\Omega_{m,0}$ is broken, as demonstrated by the green and purple contours. Instead, a correlation between these parameters is revealed. This is an important degeneracy, and indeed it appears in other areas of cosmology such as in CMB measurements Kable, Addison & Bennett (2019). The core source of the correlation between these parameters comes from how the matter density of the Universe correlates with the expansion velocity. Similarly, an anti-correlation between the $H_0$ and $p_i$ parameters is revealed when the BAO data set is included.

Therefore, our analysis provided insights into the behaviour of the PN and the PN$^+$ & SH0ES data sets and the performance of different models in $f(T)$ gravity. Our results suggest that the PN$^+$ & SH0ES data set produces tighter constraints for model parameters and higher values of $H_0$ compared to the PN data set, and the inclusion of the CC and BAO data sets have a significant impact on the parameter degeneracies and tension in $H_0$. Overall, our analysis suggests that the $f(T)$ gravity models considered in this study provide a valuable framework for future investigations of modified gravity theories. We also intend to extend this work by considering CMB data frame from surveys such as the Planck Mission in order to be able to study the early phases of the Universe including analysis of the effects that such models would have on inflationary scenarios, for example.

## ACKNOWLEDGEMENTS

The authors would like to acknowledge support from the Malta Digital Innovation Authority through the IntelliVerse grant. This paper is based upon work from COST Action CA21136 *Addressing observational tensions in cosmology with systematics and fundamental physics* (CosmoVerse) supported by European Cooperation in Science and Technology (COST). This research has been carried out using computational facilities procured through the European Regional Development Fund, project no. ERDF-080 'A supercomputing laboratory for the University of Malta'. CER acknowledges the Royal Astronomical Society as FRAS 10147 and is supported by PAPIIT UNAM project TA100122.

## DATA AVAILABILITY

The data used in this study is described in detail in Section 3. For further information on the data underlying this article, contact the corresponding author who will provide any additional information.

## REFERENCES

Ade P. A. R. et al., 2016, A&A, 594, A13
Aghanim N. et al., 2018, A&A, 641, A6
Aghanim N. et al., 2020, A&A, 641, A6
Alam S. et al., 2017, MNRAS, 470, 2617
Aldrovandi R., Pereira J. G., 2013, Teleparallel Gravity: An Introduction. Springer, Dordrecht
Amaro-Seoane P., Audley H. et al., 2017, preprint (arXiv:1702.00786)
Anagnostopoulos F. K., Basilakos S., Saridakis E. N., 2019, Phys. Rev. D, 100, 083517
Bahamonde S., Böhmer C. G., Wright M., 2015, Phys. Rev. D, 92, 104042
Bahamonde S., Flathmann K., Pfeifer C., 2019, Phys. Rev. D, 100, 084064
Bahamonde S., Levi Said J., Zubair M., 2020, J. Cosmol. Astropart. Phys., 2020, 024
Bahamonde S. et al., 2021, Rept. Prog. Phys., 86, 026901
Bahamonde S., Golovnev A., Guzmán M.-J., Said J. L., Pfeifer C., 2022, J. Cosmol. Astropart. Phys., 2022, 037
Baker J. et al., 2019, BAAS, 51, 77
Barack L. et al., 2019, Class. Quantum Gravity, 36, 143001
Baudis L., 2016, J. Phys. G: Nucl. Part. Phys., 43, 044001
Benetti M., Capozziello S., Lambiase G., 2020, MNRAS, 500, 1795
Bengochea G. R., Ferraro R., 2009, Phys. Rev., D79, 124019
Bernal J. L., Verde L., Riess A. G., 2016, J. Cosmol. Astropart. Phys., 2016, 019
Bertone G., Hooper D., Silk J., 2005, Phys. Rep, 405, 279
Beutler F. et al., 2011, MNRAS, 416, 3017
du Mas des Bourboux H. et al., 2017, A&A, 608, A130
Briffa R., Escamilla-Rivera C., Said Levi J., Mifsud J., Pullicino N. L., 2022, Eur. Phys. J. Plus, 137, 532
Brout D. et al., 2022a, ApJ, 938, 110
Brout D. et al., 2022b, ApJ, 938, 111
Cai Y.-F., Capozziello S., De Laurentis M., Saridakis E. N., 2016, Rep. Prog. Phys., 79, 106901
Chen S.-H., Dent J. B., Dutta S., Saridakis E. N., 2011, Phys. Rev., D83, 023508
Clifton T., Ferreira P. G., Padilla A., Skordis C., 2012, Phys. Rep., 513, 1
Colgáin E. O., Sheikh-Jabbari M. M., Solomon R., Bargiacchi G., Capozziello S., Dainotti M. G., Stojkovic D., 2022, Phys. Rev. D, 106, L041301
Conley A. et al., 2011, ApJS., 192, 1
Copeland E. J., Sami M., Tsujikawa S., 2006, Int. J. Mod. Phys. D, 15, 1753
Dainotti M. G., De Simone B., Schiavone T., Montani G., Rinaldi E., Lambiase G., 2021, ApJ., 912, 150
Deng X.-M., 2018, Class. Quantum Gravity, 35, 175013
Di Valentino E. et al., 2021a, Class. Quantum Gravity
Di Valentino E. et al., 2021b, Astropart. Phys., 131, 102605
Farrugia G., Levi Said J., 2016, Phys. Rev. D, 94, 124054
Farrugia G., Levi Said J., Ruggiero M. L., 2016, Phys. Rev. D, 93, 104034
Farrugia G., Levi Said J., Finch A., 2020, Universe, 6, 34
Ferraro R., Fiorini F., 2007, Phys. Rev., D75, 084031
Ferraro R., Fiorini F., 2008, Phys. Rev., D78, 124019
Finch A., Said J. L., 2018, Eur. Phys. J. C, 78, 560

Fixsen D. J., 2009, ApJ, 707, 916
Foreman-Mackey D., Hogg D. W., Lang D., Goodman J., 2013, PASP, 125, 306
Freedman W. L. et al., 2019, ApJ, 882, 34
Gaitskell R. J., 2004, Annu. Rev. Nucl. Part. Sci., 54, 315
Hayashi K., Shirafuji T., 1979, Phys. Rev. D, 19, 3524
Hohmann M., Järv L., Krššák M., Pfeifer C., 2019, Phys. Rev. D, 100, 084002
Iorio L., Saridakis E. N., 2012, MNRAS, 427, 1555
de Jaeger T., Stahl B. E., Zheng W., Filippenko A. V., Riess A. G., Galbany L., 2020, MNRAS, 496, 3402
Jimenez R., Loeb A., 2002, ApJ, 573, 37
Jimenez R., Verde L., Treu T., Stern D., 2003, ApJ, 593, 622
Kable J. A., Addison G. E., Bennett C. L., 2019, ApJ, 871, 77
Krishnan C., Colgáin E. O., Sheikh-Jabbari M. M., Yang T., 2021, Phys. Rev. D, 103, 103509
Krssak M., van den Hoogen R. J., Pereira J. G., Böhmer C. G., Coley A. A., 2019, Class. Quantum Gravity, 36, 183001
Krššák M., Saridakis E. N., 2016, Class. Quantum Gravity, 33, 115009
Linder E. V., 2009, Phys. Rev. D, 80, 123528
Linder E. V., 2010, Phys. Rev., D81, 127301
Malekjani M., Conville R. M., Colgáin E. O., Pourojaghi S., Sheikh-Jabbari M. M., 2023, preprint (arXiv:2301.12725)
Misner C. W., Thorne K. S., Wheeler J. A., 1973a, Gravitation. W. H. Freeman, San Francisco
Moresco M., 2015, MNRAS, 450, L16
Moresco M. et al., 2012, J. Cosmol. Astropart. Phys., 2012, 006
Moresco M. et al., 2016, J. Cosmol. Astropart. Phys., 2016, 014
Nakahara M., 2003, Graduate student series in physics, Geometry, Topology and Physics, 2nd edn. Taylor and Francis, London
Nesseris S., Basilakos S., Saridakis E. N., Perivolaropoulos L., 2013, Phys. Rev. D, 88, 103010
Nunes R. C., Pan S., Saridakis E. N., 2018, Phys. Rev. D, 98, 104055
Paliathanasis A., Levi Said J., Barrow J. D., 2018, Phys. Rev. D, 97, 044008
Peebles P. J. E., Ratra B., 2003, Rev. Mod. Phys., 75, 559
Pesce D. W. et al., 2020, ApJL, 891, L1
Ren X., Yan S.-F., Zhao Y., Cai Y.-F., Saridakis E. N., 2022, ApJ, 932, 2
Rezaei Akbarieh A., Izadi Y., 2019, Eur. Phys. J. C, 79, 366
Riess A. G., 2019, Nature Rev. Phys., 2, 10
Riess A. G., Casertano S., Yuan W., Macri L. M., Scolnic D., 2019, ApJ, 876, 85
Riess A. G. et al., 2022, ApJL, 934, L7
Ross A. J., Samushia L., Howlett C., Percival W. J., Burden A., Manera M., 2015, MNRAS, 449, 835
Saridakis E. N. et al., 2021, Modified Gravity and Cosmology, Springer International Publishing
Scolnic D. M. et al., 2018a, ApJ, 859, 101
Scolnic D. M. et al., 2018b, ApJ, 859, 101
Scolnic D. et al., 2022, ApJ, 938, 113
Simon J., Verde L., Jimenez R., 2005, Phys. Rev. D, 71, 123001
Sotiriou T. P., Faraoni V., 2010, Rev. Mod. Phys., 82, 451
Stern D., Jimenez R., Verde L., Kamionkowski M., Stanford S. A., 2010, J. Cosmol. Astropart. Phys., 2010, 008
Tamanini N., Boehmer C. G., 2012, Phys. Rev. D, 86, 044009
Weinberg S., 1989, Rev. Mod. Phys., 61, 1
Weitzenböock R., 1923, Invariantentheorie. Noordhoff, Gronningen
Wong K. C. et al., 2019, MNRAS
Zhang C., Zhang H., Yuan S., Liu S., Zhang T.-J., Sun Y.-C., 2014, Res. Astron. Astrophys., 14, 1221
Zhao G.-B. et al., 2019, MNRAS, 482, 3497

## APPENDIX A: ΛCDM MODEL

In Section 5, we provide comparisons between all $f_i$ models and the respective ΛCDM MCMC runs. To this end, we provide here the results for ΛCDM. The plot in Fig. A1 display the posterior distributions ad confidence regions for the different combinations of data sets. The precise values of such runs are shown in Table A1, in which as expected convergence for each data set combination occurs very fast giving nearly Gaussian uncertainties in each case.

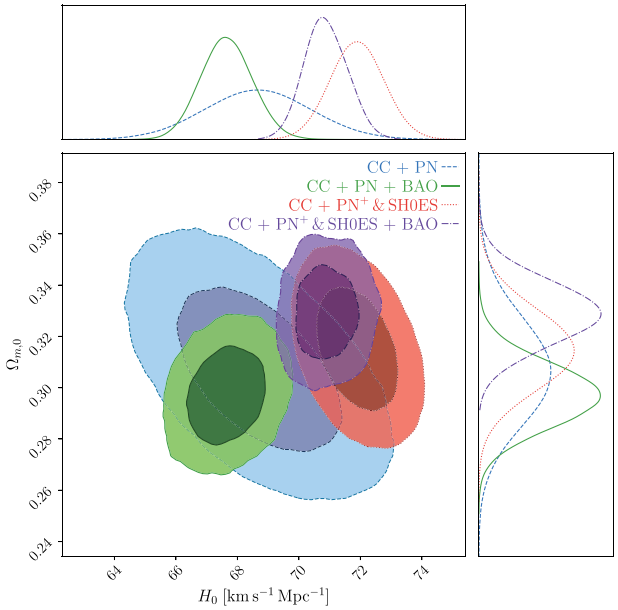


**Figure A1.** Confidence contours and posteriors for ΛCDM for the parameters $H_0$ and $\Omega_{m,0}$. The blue and green contours represent data set combinations that include PN data set, while the red and purple contours show combinations that also include the PN$^+$ & SH0ES data sets.

**Table A1.** Results for the ΛCDM model, where the first column lists the data sets used to constrain the parameters. The second to fourth columns display the constrained parameters, namely $H_0$, $\Omega_{m,0}$, and the nuisance parameter $M$.

| Data sets | $H_0$ [km s$^{-1}$ Mpc$^{-1}$] | $\Omega_{m,0}$ | $M$ |
|---|---|---|---|
| CC+PN | $68.6^{+1.8}_{-1.7}$ | $0.306 \pm 0.021$ | $-19.383^{+0.050}_{-0.053}$ |
| CC+PN+BAO | $67.59^{+0.89}_{-0.81}$ | $0.297 \pm 0.013$ | $-19.419^{+0.026}_{-0.033}$ |
| CC+PN$^+$ & SH0ES | $71.88^{+0.88}_{-0.87}$ | $0.315 \pm 0.016$ | $-19.298 \pm 0.025$ |
| CC +PN$^+$ & SH0ES+BAO | $70.76^{+0.80}_{-0.64}$ | $0.329 \pm 0.013$ | $-19.326^{+0.024}_{-0.022}$ |

## APPENDIX B: PN$^+$ & SH0ES PARAMETER CONSTRAINTS

To investigate the impact of the different data set combinations on the $H_0$ tension, we performed an MCMC analysis using only the PN$^+$ & SH0ES data set as well. We then compared the deviation in units of $\sigma$ between the resulting $H_0$ values for each model and each data set combination with that of P18, as shown in Fig. 5. The constrained parameter values for each model obtained from this MCMC analysis are presented in Table B1.

**Table B1.** Results for the constrained parameters using the PN$^+$ & SH0ES data set for each model considered in the analysis section.

| Model | $H_0$ [km s$^{-1}$ Mpc$^{-1}$] | $\Omega_{m,0}$ | $p_i$ | $M$ |
|---|---|---|---|---|
| ΛCDM | $73.4 \pm 1.1$ | $0.334^{+0.021}_{-0.020}$ | – | $-19.247 \pm 0.033$ |
| $f_1$CDM | $73.3 \pm 1.0$ | $0.331^{+0.044}_{-0.070}$ | $0.28^{+0.22}_{-0.37}$ | $-19.248^{+0.030}_{-0.029}$ |
| $f_2$CDM | $73.2^{+1.1}_{-1.0}$ | $0.318^{+0.023}_{-0.102}$ | $0.33^{+0.32}_{-0.26}$ | $-19.259^{+0.044}_{-0.021}$ |
| $f_3$CDM | $73.2 \pm 1.1$ | $0.308^{+0.032}_{-0.099}$ | $0.33^{+0.34}_{-0.24}$ | $-19.225^{+0.040}_{-0.085}$ |

## APPENDIX C: MCMC ANALYSIS PRIORS

The MCMC analyses were conducted with Gaussian distributions over the priors. The common parameters assume common prior ranges with the Hubble constant given by $50 < H_0 < 100$, while the matter density parameter takes on the range $0.1 < \Omega_{m,0} < 0.9$. On the other hand, the model specific parameters take on the following ranges:

$$-1 < p_1 < 1\,, \tag{C1}$$

$$0 < p_2 < 1\,, \tag{C2}$$

$$0 < p_3 < 1\,. \tag{C3}$$

This paper has been typeset from a TEX/LATEX file prepared by the author.